Observation of cnoidal wave localization in nonlinear topolectric circuits

Hendrik Hohmann [1] Tobias Hofmann [1] Tobias Helbig [1] Stefan Imhof,[2] Hauke Brand [2] Lavi K. Upreti [1,3]
Alexander Stegmaier [1] Alexander Fritzsche,[1] Tobias Müller [1] Udo Schwingenschlögl,[4] Ching Hua Lee [5]
Martin Greiter [1] Laurens W. Molenkamp,[2] Tobias Kießling,[2] and Ronny Thomale [1,*]

[1]*Institute for Theoretical Physics and Astrophysics, University of Würzburg, 97074 Würzburg, Germany*
[2]*Physikalisches Institut, Universität Würzburg, 97074 Würzburg, Germany*
[3]*Universität Konstanz, Fachbereich Physik, 78457 Konstanz, Germany*
[4]*Physical Sciences and Engineering Division (PSE), King Abdullah University of Science and Technology (KAUST),
Thuwal 23955-6900, Saudi Arabia*
[5]*Department of Physics, National University of Singapore, 117542, Singapore*

We observe a localized cnoidal (LCn) state in an electric circuit network. Its formation derives from the interplay of nonlinearity and the topology inherent to a Su-Schrieffer-Heeger (SSH) chain of inductors. Varicap diodes act as voltage-dependent capacitors, and create a nonlinear on-site potential. For a sinusoidal voltage excitation around midgap frequency, we show that the voltage response in the nonlinear SSH circuit follows the Korteweg-de Vries equation. The topological SSH boundary state, which relates to a midgap impedance peak in the linearized limit is distorted into the LCn state in the nonlinear regime, where the cnoidal eccentricity decreases from edge to bulk.

Introduction. Since the first observation of a solitary wave in a canal near Edinburgh by Russel in 1834, solitons as special solutions to nonlinear equations of motion have been studied extensively [1–3]. The phenomenon has subsequently gained relevance for a multitude of mathematical, biological, and physical domains [4–7]. It includes, but is not exhausted by, hydrodynamic waves in oceans, rivers, and the atmosphere [8–10], ion-acoustic solitons in plasma [11], and DNA fluctuations [5]. The ability to analytically retrace the soliton has stimulated new developments in optical fiber communications [12–14] and solid-state physics [15], which culminated in the modeling of electrical conductance in polymers through the Su-Schrieffer-Heeger (SSH) model [16]. There, the conductivity of trans-polyacetylene derives from charged solitons, propagating as domain walls between two allowed energy configurations [17,18]. Initially investigated in the nonlinear soliton regime, a linearized description of the dimerized SSH model (cf. Supplemental B [19]) subsequently gained importance as a toy model and building block for symmetry-protected boundary modes and topological phases. In some aspects, the SSH model can be thought of as the cradle of topological classifications, which has substantially deepened the understanding of topological states of matter [20,21]. Physical implications of dimerization are not limited to boundary obstructed topological phases [22] but play a major role in a variety of physical systems such as quantum antiferromagnets [23–25] and fullerenes [26–28].

Many of the topological phases known to date are not reserved to quantum systems, but rather have additionally or exclusively been realized in classical metamaterials [29], such as mechanic [30], acoustic [31,32], photonic [33,34], and electric [35,36] setups. Furthermore, metamaterials have been employed to investigate effects caused by nonlinearity, which is either inherent to the platform, e.g., Kerr nonlinearity in optical materials [37], or added to the setup by nonlinear components [38,39]. Here, topolectric circuits [40] stand out in terms of versatility and accessibility, as they are capable of realizing both discrete (lattice type) and continuous (transmission line) systems in the short and long wavelength limit, respectively. Both regimes have been explored experimentally, from topological phases [41,42] and band structures [43,44] to solitons [38,39,45,46] and cnoidal waves as periodic soliton-like solutions of the Korteweg-de Vries (KdV) equation [2,47,48]. Moreover, the availability of commercially refined nonlinear electronic components, such as nonlinear resistors [49] or varicap diodes [38], renders electric circuits ideally suited to study the interplay of topology and nonlinearity [50–54].

In this Letter, we investigate a nonlinear SSH circuit. In contrast to previous works, where the nonlinearity enters in the kinetic term [50–53], we introduce it as a local potential. As a response to a sinusoidal voltage excitation at midgap frequencies fed into the edge of the circuit, we measure the localized cnoidal (LCn) state. Originating from the intertwining of topological localization and nonlinearity, the LCn state shows an exponential decay of its root mean square (RMS) amplitude towards the bulk, whereas the nonlinearity manifests itself in a temporal distortion of the
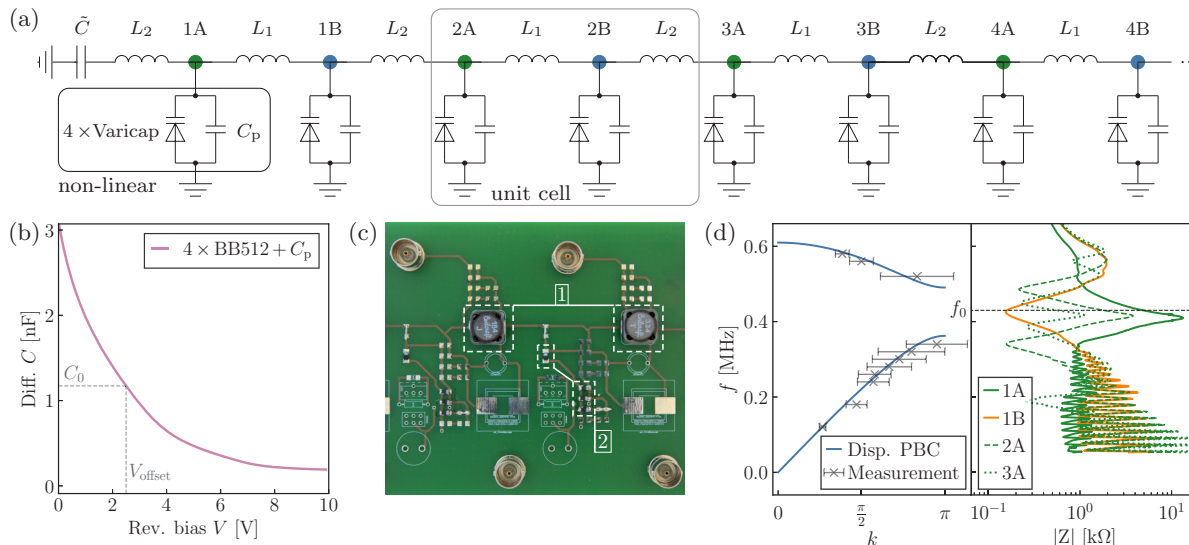

FIG. 1. (a) Schematic of the nSSH circuit. Alternating inductances L_1 and L_2 connect the voltage nodes, reverse-biased varicap diodes to ground act as nonlinear capacitances and the parallel capacitor C_p takes the parasitic influence of the measurement setup into account [19]. $\tilde{C} \gg C(V_{offset})$ blocks the dc voltage offset. The gray rectangle depicts one unit cell. (b) Measurement of the voltage dependence of the four Siemens BB512 varicap diodes in parallel configuration and C_p. (c) One unit cell of the nSSH circuit on the PCB with [1] inductors of nominal values $L_{1,nom} = 330\,\mu H$ and $L_{2,nom} = 180\,\mu H$, and [2] varicap diodes. (d) (left) Theoretical (blue curve) and measured (gray crosses) dispersion relation for PBC in the linear limit at the operating point $V_{offset} = 2.5\,V$. (right) Small signal impedance analysis between nodes 1A, 1B, 2A, 3A and ground for OBC. An impedance peak at the midgap frequency $f_0 = 430\,kHz$ indicates the localized SSH boundary state.

sinusoidal character of the input. We develop an approach to theoretically describe the LCn state by separating the chain into decoupled LC resonators, which are described by the KdV equation and its cnoidal wave solutions. Our findings establish circuit networks as the platform of choice to explore nonlinear topological matter.

Nonlinear SSH circuit. We create a nonlinear SSH (nSSH) circuit, schematically depicted in Fig. 1(a), in which alternating inductances L_1 and L_2 connect the circuit nodes. Each node in the two-site unit cell is grounded by a parallel configuration of four varicap diodes of type Siemens BB512 in reverse-bias setting and a linear capacitor C_p. They realize a nonlinear on-site capacitance and extend the linear SSH model to the nonlinear regime. C_p is added to the theoretical model to account for parasitic capacitances induced by the measurement setup. In a topolectric circuit, the elements connecting the nodes correspond to hopping terms in a tight-binding model, while the connections to ground mimic an on-site energy. From the actual printed circuit board (PCB) with a total of 25 unit cells and 50 voltage nodes, a cutout of one unit cell is shown in Fig. 1(c). Since the varicap diodes would be conductive for negative node voltages, we operate the circuit at positive voltages in the depletion region. This is achieved by applying a dc voltage offset V_{offset} to all nodes, which defines the operating point of the nonlinear capacitance $C_0 = C(V_{offset})$. In order to experimentally stabilize the voltage offset, the nodes at the edges are decoupled from ground by a large additional capacitor $\tilde{C} \gg C_0$, which does not affect the dynamical behavior of the system. The total differential capacitance $C(V)$ from each node to ground decreases nonlinearly as a function of the reverse biased voltage V, measured in Fig. 1(b). In addition to the voltage offset,

we excite the nSSH circuit with an ac voltage signal yielding a total input voltage $V(t) = V_{offset} + A_0 \sin(\omega t)$. In this passive circuit, the effect of the nonlinearity on the voltages and currents increases with larger excitation amplitudes A_0. This allows us to employ the amplitude of the ac input signal as a tuning parameter for the influence of the nonlinear on-site capacitance on the circuit.

Linear limit of the nSSH circuit. To connect the spatial character of the LCn state to the description of the nSSH circuit in its linear limit, we employ a small amplitude signal analysis. For small ac input signals ($A_0 \ll V_{offset}$), we assume the on-site capacitance to be constant, $C(V) \approx C_0$, and linearize the equations of motion (EOM) around the operating point V_{offset} to obtain an effective description in the linear limit. The linearized EOM are diagonal in frequency space and their solutions are characterized by the dispersion relation.

The effective linear model is equivalent to the SSH chain, and the dispersion relation $\omega(k)$ for periodic boundary conditions (PBC) is given by

$$\omega_{\pm}^2(k) = \omega_0^2 \pm \frac{1}{C_0}\sqrt{\frac{1}{L_1^2} + \frac{1}{L_2^2} + \frac{2}{L_1 L_2}\cos(k)}, \quad (1)$$

with $\omega_0^2 = C_0^{-1}(L_1^{-1} + L_2^{-1}) \equiv (2\pi f_0)^2$. We set $L_1 > L_2$ to tune the circuit into the topological regime.

We measure the dispersion relation $\omega(k)$ in the nSSH circuit by reading out one wavelength of the real-space voltage distribution resulting from a small signal excitation with frequency ω [cf. left part of Fig. 1(d)]. Due to the finite resolution in real space, the precision decreases for $k \to \pi$. In the right part of Fig. 1(d) we depict a frequency-resolved small-signal impedance measurement between nodes close to the boundary
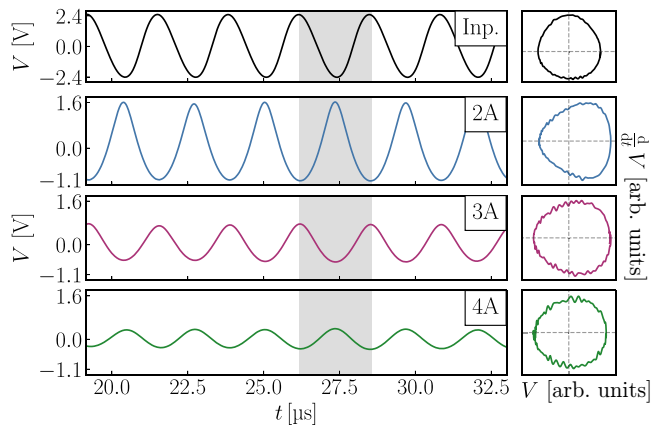
FIG. 2. ac measurement of the LCn state at $V_{\mathrm{offset}} = 2.5$ V. (top) Sinusoidal input signal with frequency $f_0 = 430$ kHz and amplitude $A_0 = 2.5$ V fed into node 1A. (left) Steady-state voltage response at nodes 2A, 3A, and 4A starting at $t \approx 18\,\mu$s. The sinusoidal input is deformed into the LCn state, where amplitude and eccentricity decrease from edge to bulk. (right) Phase space plot of one period of the voltage signal [indicated by the gray area in (a)], visualizing its deformation.

and ground for open boundary conditions (OBC). Within the two branches of the dispersion relation, we identify several impedance peaks corresponding to the individual bulk modes of the finite circuit network. Our measurements reveal the boundary state of the SSH model at the midgap frequency f_0, featuring localization on sublattice A at the edge and exponential decay towards the bulk.

Continuum limit: Nonlinear transmission line. The complete nonlinear circuit EOM at large input amplitudes A_0 on the order of V_{offset} can not be solved exactly. A standard approach is to apply a continuum approximation by placing oneself in the lower branch of the dispersion in Fig. 1(d) close to $k = 0$ with no phase shift between sublattice sites. In this low-energy, long-wavelength limit, the dimerization and discrete lattice character are no longer relevant and the circuit setup realizes a nonlinear transmission line [45]. The EOM resemble the KdV equation (cf. Supplemental A [19]), for which a bell-shaped excitation leads to the formation of a pulse soliton [39]. It propagates with constant shape and velocity through the transmission line, because the defocusing effect of the dispersion relation is compensated by the nonlinearity. This approach fails for regions close to the band gap. The phase shift of π between adjacent unit cells as well as the suppressed signal on sublattice B in the topological midgap state invalidate the continuum approximation.

Dimerized nSSH circuit: Localized cnoidal state. We excite the nSSH circuit with a sinusoidal signal of midgap frequency f_0 at the boundary and measure the voltage response once a steady state is reached. With the localization on sublattice A in the linear topological edge state, nonlinear effects are strongly suppressed at sublattice B, resulting in their on-site amplitudes to remain small even for large A_0 (cf. Supplemental C [19]). Figure 2 shows the voltage response of sublattice nodes A to a sinusoidal excitation at node 1A in

the nonlinear regime ($A_0 = 2.5$ V). We identify this voltage configuration with spatial localization at the boundary in the nonlinear regime as the LCn state. The effect of nonlinearity manifests itself in the temporal distortion of the sinusoidal signal at nodes of sublattice A: The phase space plots on the right side of Fig. 2 show how the voltage response is deformed as compared to the elliptic shape of the input signal. The eccentricity, a parameter characterizing the signal distortion with respect to a sinusoidal wave, decreases towards the bulk.

As the frequency f_0 of the driving sets the period of the voltage response in the whole circuit, each waveform is composed of higher harmonics at integer multiples of this base frequency. Due to the band gap around f_0 and since there are no dispersive states at higher harmonics of f_0, it is the LCn mode that is excited predominantly.

Theoretical description of the LCn state. Given the small ac amplitude of sublattice nodes B in the midgap state, we can approximate them as being replaced by ac ground, as shown in Fig. 3(a). This decouples the chain into a set of independent single resonators, reducing the full nonlinear differential equations to a local homogeneous subset (cf. Supplemental C, D [19]). The amplitude remains as an undetermined parameter in the solution of the reduced EOM and is specified by the spatial voltage profile of the LCn state. Exemplified in Fig. 3(a) for node 2A, each single resonator can be recast as an LC circuit with inductance $L = (L_1^{-1} + L_2^{-1})^{-1}$ and nonlinear capacitance $C(V)$.

In the linear limit, the resonance frequency of the single resonator matches that of the midgap SSH edge state with $f_0 = 1/(2\pi\sqrt{LC_0})$. This originates from the dimerized regime of the tight-binding model, where the topological state resides at zero energy within the band gap. The analogous scale of zero energy in electric circuits is given by the midgap frequency f_0.

To analytically trace the nonlinear differential equations of the single resonator, we model the voltage-dependent differential capacitance by the equation for an abrupt p-n junction. The varicap capacitance is given by the voltage-dependent size of the depletion region between p- and n-doped area of the diode (cf. Supplemental D [19]). At voltages V close to V_{offset} this results in an inverted square root law [55]

$$C(V) \approx \frac{\mathcal{C}}{\sqrt{1 + \frac{V - \nu}{\phi}}}, \tag{2}$$

where ϕ, $\mathcal{C}$, and ν are fitted to resemble the measured capacitance in Fig. 1(b) (cf. Supplemental D [19]). $\mathcal{C}$ can be interpreted as the zero bias junction capacitance and ϕ as the total potential difference across the junction.

Since we are only interested in its ac contribution, we decompose the voltage as $V(t) = V_{\mathrm{offset}} + u(t)$. The nonlinear relation $Q[u(t)]$ between the charge $Q(t)$ accumulated on the capacitor and the voltage $u(t)$ across it is obtained by integrating Eq. (2) using $dQ = C(V)dV$. Inserting the inverted function $u[Q(t)]$ into the standard differential equation for the LC resonator, we find that the charge $Q(t)$ follows the KdV equation in its stationary limit [56]. The periodic solutions for $Q(t)$ are given by cnoidal waves [57], which can be regarded as a periodic arrangement of single solitons. With the relation
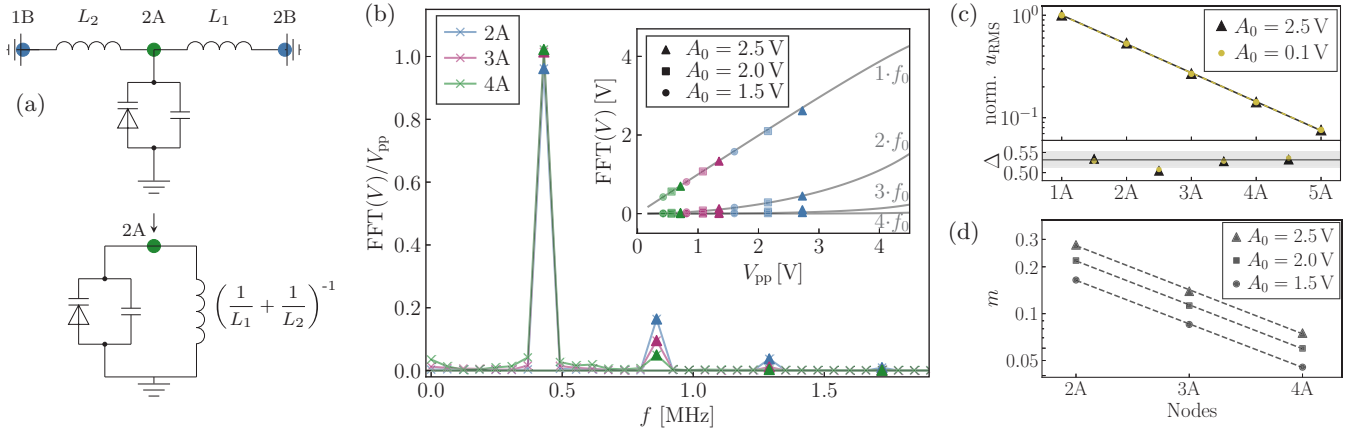
FIG. 3. (a) Transformation of a segment of the nSSH circuit to a nonlinear LC resonator by treating the sublattice nodes B as virtual ground, due to their negligible amplitude in the LCn state. (b) Discrete Fourier transformation of the measured voltage response in the LCn state at first three sublattice A nodes (color encoded), normalized with respect to the peak to peak voltage V_{pp}. The crosses mark the evaluated values, guided by solid lines and with triangles at multiples of the base frequency f_0. Due to nonlinear effects, higher harmonics of the fundamental frequency $f_0 = 430$ kHz are excited. The inset compares the Fourier components for different excitation amplitudes A_0 (marker encoded), and nodes 2A, 3A, and 4A, with the analytical solution in Eq. (3), depicted as gray lines. (c) Logarithmic plot of the normalized RMS voltage for the linear and nonlinear case with respective linear fits. The ratio Δ between subsequent RMS values together with the theoretically expected value in gray is shown below. (d) Logarithmic plot of the eccentricity m for different excitation amplitudes A_0 with linear fits.

$u[Q(t)]$, we obtain the analytic description of the ac voltage

$$u(t) = \frac{1}{4\,\mathcal{C}^2\,\phi} \left[\eta\,(\eta + 2\Theta) + 2A_Q\,(\eta + \Theta)\,\mathrm{cn}^2(\mu t\,|\,m) \right.$$
$$\left. + A_Q^2\,\mathrm{cn}^4(\mu t\,|\,m) \right], \tag{3}$$

where $\mathrm{cn}(x\,|\,m)$ denotes the Jacobi elliptic cosine function, $m \in [0, 1]$ the eccentricity of the wave, and Θ a system-dependent constant. For the functional dependencies of the valley elevation $\eta(m)$, the peak to peak amplitude $A_Q(m)$ of the cnoidal wave solution $Q(t)$, the elliptic frequency $\mu(m)$ on the parameter m, and a full derivation refer to Supplemental Material D [19]. The period of $\mathrm{cn}^2(\mu t\,|\,m)$ is $T = 2K(m)/\mu(m)$ and fixed by the external input frequency f_0. $K(m)$ denotes the complete elliptic integral of the first kind. For eccentricities up to $m \approx 0.3$, the eigenfrequency of the single resonator $f(m) = 1/T(m)$ is approximately constant and matches the excitation frequency (cf. Supplemental D [19]). Hence, the solution Eq. (3) applies to the driven setup.

In Fig. 3(b) we perform a discrete Fourier transformation of the measured steady state for an input amplitude A_0 of 2.5 V. Due to the nonlinearity, higher harmonics of the fundamental frequency f_0 are excited, albeit with smaller amplitude. In agreement with the time scale induced by the driving, the EOM for the single resonator allow for solutions, which are composed of excitations at multiples of the base frequency f_0. As shown in the inset of Fig. 3(b), the measured data agrees with the Fourier coefficients of the theoretical ac voltage solution in Eq. (3) depicted in gray. The spatially resolved normalized RMS value u_{RMS} of the LCn state is shown in Fig. 3(c) and compared to the linear limit. It decreases exponentially towards the bulk with $u_{RMS} \propto \Delta^x$ with the same attenuation factor Δ in the linear and nonlinear regime, where x denotes the number of unit cells counted from the

edge. The mean experimental values are $\Delta_{lin} = 0.5237(17)$ and $\Delta_{n\text{-}lin} = 0.5226(16)$, $0.5230(17)$, $0.5227(18)$ for $A_0 = 0.1$ V and $A_0 = 1.5$V, 2.0V, 2.5V, respectively. The nominal value is in the range of $\Delta_{nom} = L_2/L_1 = 0.513 \ldots 0.551$ resulting from the precharacterization of inductors with $L_1 = 334 \ldots 343\,\mu$H and $L_2 = 176 \ldots 184\,\mu$H measured at $f = 430$ kHz. The experimentally obtained values for the attenuation factor agree with the theoretical expectation of the linear limit. We hence confirm that the LCn state inherits the spatial behavior, and thus its topological character, from the boundary state in the linearized SSH limit. In contrast to the peak-to-peak voltage, the spatial profile of the RMS value, and accordingly the reactive power at each node, remains invariant upon the introduction of nonlinearity (cf. Supplemental C [19]). Locally at each node, the RMS value determines the parameter m of the cnoidal wave solution in Eq. (3) and traces all parameters back to the input. Figure 3(d) shows the spatial decay of the eccentricity m towards the bulk obtained by solving the peak-to-peak voltage of the signal $u_{pp} = u(0) - u(T/2)$ for m. With larger voltage amplitudes close to the boundary of the circuit the influence of the nonlinearity is stronger, and we expect a greater deformation of the wave. In agreement with Fig. 2, as m increases towards the boundary, the peaks of the wave become sharper while the valleys get wider. This is reflected in the attenuation factor of the exponential decay of m, which is measured to be $\Delta_m = 0.5249(25)$, $0.5221(33)$, $0.5209(65)$ for excitation amplitudes of $A_0 = 1.5$V, 2.0V, 2.5V, respectively, and matches with the decay factor of u_{RMS}.

Conclusion. Our one-dimensional periodic circuit network with Su-Schrieffer-Heeger type dimerization and on-site nonlinearity exhibits an unprecedented topological voltage configuration, which we denote as the localized cnoidal state. The interplay of topological edge modes and nonlinearity is probed within an experimental framework of exceptional accessibility and tunability. Using a single-resonator

approximation, we find that the Korteweg-de Vries equation with cnoidal wave solutions determines the waveform in the time domain. Intriguingly, the eccentricity, i.e., the deformation of the waveform due to the nonlinearity, also decays exponentially from edge to bulk. The topological character of the boundary mode in the strongly nonlinear SSH regime suggests itself for further analysis, and might allow us to acquire a deeper understanding of nonlinear topological matter.

[1] J. S. Russell, Report on waves, in *Report of the Fourteenth Meeting of the British Association for the Advancement of Science held at York in September 1844* (John Murray, London, 1845).

[2] D. J. Korteweg and G. de Vries, XLI. On the change of form of long waves advancing in a rectangular canal, and on a new type of long stationary waves, Philos. Mag. **39**, 422 (1895).

[3] A. C. Scott, F. Y. F. Chu, and D. W. McLaughlin, The soliton: A new concept in applied science, Proc. IEEE **61**, 1443 (1973).

[4] M. J. Ablowitz and H. Segur, *Solitons and the Inverse Scattering Transform* (SIAM, Philadelphia, 1981).

[5] S. Yomosa, Soliton excitations in deoxyribonucleic acid (DNA) double helices, Phys. Rev. A **27**, 2120 (1983).

[6] T. Heimburg and A. D. Jackson, On soliton propagation in biomembranes and nerves, Proc. Natl. Acad. Sci. USA **102**, 9790 (2005).

[7] R. Appali, U. van Rienen, and T. Heimburg, A comparison of the Hodgkin–Huxley model and the soliton theory for the action potential in nerves, in *Advances in Planar Lipid Bilayers and Liposomes*, Vol. 16, edited by Aleš Iglič (Academic Press, New York, 2012), Chap. 9, pp. 275–299.

[8] A. R. Osborne and T. L. Burch, Internal solitons in the Andaman sea, Science **208**, 451 (1980).

[9] D. K. Lynch, Tidal bores, Sci. Am. **247**, 146 (1982).

[10] J. P. Boyd, Equatorial solitary waves. Part I: Rossby solitons, J. Phys. Oceanogr. **10**, 1699 (1980).

[11] K. E. Lonngren, Soliton experiments in plasmas, Plasma Phys. **25**, 943 (1983).

[12] A. Hasegawa and F. Tappert, Transmission of stationary nonlinear optical pulses in dispersive dielectric fibers. I. Anomalous dispersion, Appl. Phys. Lett. **23**, 142 (1973).

[13] P. Emplit, J. P. Hamaide, F. Reynaud, C. Froehly, and A. Barthelemy, Picosecond steps and dark pulses through nonlinear single mode fibers, Opt. Commun. **62**, 374 (1987).

[14] H. A. Haus and W. S. Wong, Solitons in optical communications, Rev. Mod. Phys. **68**, 423 (1996).

[15] J. Denschlag, J. E. Simsarian, D. L. Feder, C. W. Clark, L. A. Collins, J. Cubizolles, L. Deng, E. W. Hagley, K. Helmerson, W. P. Reinhardt, S. L. Rolston, B. I. Schneider, and W. D. Phillips, Generating solitons by phase engineering of a Bose-Einstein condensate, Science **287**, 97 (2000).

[16] W. P. Su, J. R. Schrieffer, and A. J. Heeger, Solitons in Polyacetylene, Phys. Rev. Lett. **42**, 1698 (1979).

[17] W. P. Su, J. R. Schrieffer, and A. J. Heeger, Soliton excitations in polyacetylene, Phys. Rev. B **22**, 2099 (1980).

[18] A. J. Heeger, S. Kivelson, J. R. Schrieffer, and W. P. Su, Solitons in conducting polymers, Rev. Mod. Phys. **60**, 781 (1988).

[19] See Supplemental Material at http://link.aps.org/supplemental/10.1103/PhysRevResearch.5.L012041 for a revision of the Korteweg-de Vries equation, and the topological Su-Schrieffer-Heeger model, a detailed analysis of the spatial character of the LCn state, a derivation of the single resonator model, and a description of the experimental circuit setup

[20] X.-L. Qi and S.-C. Zhang, Topological insulators and superconductors, Rev. Mod. Phys. **83**, 1057 (2011).

[21] M. Z. Hasan and C. L. Kane, Colloquium: Topological insulators, Rev. Mod. Phys. **82**, 3045 (2010).

[22] E. Khalaf, W. A. Benalcazar, T. L. Hughes, and R. Queiroz, Boundary-obstructed topological phases, Phys. Rev. Res. **3**, 013239 (2021).

[23] S. Sachdev and R. N. Bhatt, Bond-operator representation of quantum spins: Mean-field theory of frustrated quantum Heisenberg antiferromagnets, Phys. Rev. B **41**, 9323 (1990).

[24] B. Sriram Shastry and B. Sutherland, Exact ground state of a quantum mechanical antiferromagnet, Physica B+C **108**, 1069 (1981).

[25] P. Ghosh, T. Müller, and R. Thomale, Another exact ground state of a two-dimensional quantum antiferromagnet, Phys. Rev. B **105**, L180412 (2022).

[26] Y. Hasegawa, Y. Ling, S. Yamazaki, T. Hashizume, H. Shinohara, A. Sakai, H. W. Pickering, and T. Sakurai, STM study of one-dimensional cluster formation of fullerenes: Dimerization of Y@C_{82}, Phys. Rev. B **56**, 6470 (1997).

[27] G. Gumbs, A. Iurov, A. Balassis, and D. Huang, Anisotropic plasmon-coupling dimerization of a pair of spherical electron gases, J. Phys.: Condens. Matter **26**, 135601 (2014).

[28] R. Zhang, M. Murata, T. Aharen, A. Wakamiya, T. Shimoaka, T. Hasegawa, and Y. Murata, Synthesis of a distinct water dimer inside fullerene C_{70}, Nat. Chem. **8**, 435 (2016).

[29] F. D. M. Haldane and S. Raghu, Possible Realization of Directional Optical Waveguides in Photonic Crystals with Broken Time-Reversal Symmetry, Phys. Rev. Lett. **100**, 013904 (2008).

[30] R. Süsstrunk and S. D. Huber, Observation of phononic helical edge states in a mechanical topological insulator, Science **349**, 47 (2015).

[31] A. Khanikaev, R. Fleury, S. Mousavi, and A. Alù, Topologically robust sound propagation in an angular-momentum-biased graphene-like resonator lattice, Nat. Commun. **6**, 8260 (2015).

[32] X. Zhang, M. Xiao, Y. Cheng, M.-H. Lu, and J. Christensen, Topological sound, Commun. Phys. **1**, 97 (2018).

[33] T. Ozawa, H. M. Price, A. Amo, N. Goldman, M. Hafezi, L. Lu, M. C. Rechtsman, D. Schuster, J. Simon, O. Zilberberg, and I. Carusotto, Topological photonics, Rev. Mod. Phys. **91**, 015006 (2019).

[34] R. Li, P. Li, Y. Jia, and Y. Liu, Self-localized topological states in three dimensions, Phys. Rev. B **105**, L201111 (2022).

[35] V. V. Albert, L. I. Glazman, and L. Jiang, Topological Properties of Linear Circuit Lattices, Phys. Rev. Lett. **114**, 173902 (2015).

[36] J. Ningyuan, C. Owens, A. Sommer, D. Schuster, and J. Simon, Time- and Site-Resolved Dynamics in a Topological Circuit, Phys. Rev. X **5**, 021031 (2015).

[37] H. S. Eisenberg, Y. Silberberg, R. Morandotti, A. R. Boyd, and J. S. Aitchison, Discrete Spatial Optical Solitons in Waveguide Arrays, Phys. Rev. Lett. **81**, 3383 (1998).

[38] D. Jäger, Experiments on KdV solitons, J. Phys. Soc. Jpn. **51**, 1686 (1982).

[39] G. Sebastiano, P. Pantano, and P. Tucci, An electrical model for the Korteweg-de Vries equation, Am. J. Phys. **52**, 238 (1984).

[40] C. H. Lee, S. Imhof, C. Berger, F. Bayer, J. Brehm, L. W. Molenkamp, T. Kiessling, and R. Thomale, Topolectrical circuits, Commun. Phys. **1**, 39 (2018).

[41] S. Imhof, C. Berger, F. Bayer, J. Brehm, L. W. Molenkamp, T. Kiessling, F. Schindler, C. H. Lee, M. Greiter, T. Neupert, and R. Thomale, Topolectrical-circuit realization of topological corner modes, Nat. Phys. **14**, 925 (2018).

[42] T. Hofmann, T. Helbig, C. H. Lee, M. Greiter, and R. Thomale, Chiral Voltage Propagation and Calibration in a Topolectrical Chern Circuit, Phys. Rev. Lett. **122**, 247702 (2019).

[43] T. Helbig, T. Hofmann, C. H. Lee, R. Thomale, S. Imhof, L. W. Molenkamp, and T. Kiessling, Band structure engineering and reconstruction in electric circuit networks, Phys. Rev. B **99**, 161114(R) (2019).

[44] Y. Lu, N. Jia, L. Su, C. Owens, G. Juzeliūnas, D. I. Schuster, and J. Simon, Probing the Berry curvature and Fermi arcs of a Weyl circuit, Phys. Rev. B **99**, 020302(R) (2019).

[45] T. Kofane, B. Michaux, and M. Remoissenet, Theoretical and experimental studies of diatomic lattice solitons using an electrical transmission line, J. Phys. C **21**, 1395 (1988).

[46] P. Marquie, J. M. Bilbault, and M. Remoissenet, Generation of envelope and hole solitons in an experimental transmission line, Phys. Rev. E **49**, 828 (1994).

[47] M. Toda, Waves in nonlinear lattice, Prog. Theor. Phys. Suppl. **45**, 174 (1970).

[48] D. L. Sekulic, M. V. Sataric, M. B. Zivanov, and J. S. Bajic, Soliton-like pulses along electrical nonlinear transmission line, Elektron. ir Elektrotech. **121**, 53 (2012).

[49] T. Kotwal, F. Moseley, A. Stegmaier, S. Imhof, H. Brand, T. Kießling, R. Thomale, H. Ronellenfitsch, and J. Dunkel, Active topolectrical circuits, Proc. Natl. Acad. Sci. USA **118**, e2106411118 (2021).

[50] Y. Hadad, A. B. Khanikaev, and A. Alù, Self-induced topological transitions and edge states supported by nonlinear staggered potentials, Phys. Rev. B **93**, 155112 (2016).

[51] Y. Hadad, J. Soric, A. Khanikaev, and A. Alù, Self-induced topological protection in nonlinear circuit arrays, Nat. Electron. **1**, 178 (2018).

[52] Y. Hadad, V. Vitelli, and A. Alu, Solitons and propagating domain walls in topological resonator arrays, ACS Photonics **4**, 1974 (2017).

[53] Y. Wang, L.-J. Lang, C. H. Lee, B. Zhang, and Y. Chong, Topologically enhanced harmonic generation in a nonlinear transmission line metamaterial, Nat. Commun. **10**, 1102 (2019).

[54] M. Ezawa, Topological edge states and bulk-edge correspondence in dimerized Toda lattice, J. Phys. Soc. Jpn. **91**, 024703 (2022).

[55] P. S. Linsay, Period Doubling and Chaotic Behavior in a Driven Anharmonic Oscillator, Phys. Rev. Lett. **47**, 1349 (1981).

[56] L. Marsh, Nonlinear dynamics of the RL-diode circuit, Ph.D. thesis, University of Surrey, 2006.

[57] K. B. Blyuss, Chaotic behaviour of solutions to a perturbed Korteweg–de Vries equation, Rep. Math. Phys. **49**, 29 (2002).